

Whole-Blood Boundary Analysis of BioFET-Based ctDNA Detection for Intravascular Sensing in Intrabody Nanonetworks

Ida Kleger-Rudomin
Gdansk University of Technology
Poland

Filip Lemic
i2Cat Foundation
Spain

Sergi Abadal
Universitat Politècnica de Catalunya
Spain

Eduard Alarcón
Universitat Politècnica de Catalunya
Spain

Ethungshan Shitiri*
Universitat Politècnica de Catalunya
Spain

Abstract

Liquid biopsy can detect tumor-derived biomarkers such as circulating tumor DNA (ctDNA), but ultra-low-fraction assays remain costly, slow, and difficult to scale. This motivates interest in intravascular *in vivo* sensing in the context of intrabody nanonetworks, where nanosensors could support local biomarker monitoring. BioFET-based nanosensors are relevant here because they are label-free, highly miniaturizable, and have shown strong ctDNA sensitivity in controlled media. We examine whether this sensitivity still yields reliable ctDNA detection in whole blood using a reduced-order stochastic simulation model that links operating-point selection, Debye-screened charge transduction, stochastic finite-capacity binding, nonspecific adsorption, background fluctuations, and intrinsic electronic noise to blank-threshold detection. Monte Carlo evaluation with physiologically grounded parameters shows that short Debye length and several-nanometer charge-to-channel separation attenuate the current shift, while low-frequency noise and background fluctuations reduce the margin between target-present and blank responses. Under the tested quasi-static charge-gating regime, the simulated current shifts do not reliably exceed the blank-derived threshold at low ctDNA concentrations. The model therefore provides a whole-blood boundary analysis that identifies which interface configurations and operating conditions most strongly limit reliable BioFET-based intravascular ctDNA detection.

CCS Concepts

• **Computing methodologies** → **Model development and analysis**; *Simulation types and techniques*; • **Computer systems organization** → *Sensors and actuators*; • **Applied computing** → *Life and medical sciences*; • **Networks** → *Cyber-physical networks*.

*Corresponding author

Permission to make digital or hard copies of all or part of this work for personal or classroom use is granted without fee provided that copies are not made or distributed for profit or commercial advantage and that copies bear this notice and the full citation on the first page. Copyrights for components of this work owned by others than the author(s) must be honored. Abstracting with credit is permitted. To copy otherwise, or republish, to post on servers or to redistribute to lists, requires prior specific permission and/or a fee. Request permissions from permissions@acm.org.

NanoCom '26, St. John's, Canada

© 2026 Copyright held by the owner/author(s). Publication rights licensed to ACM.
ACM ISBN 979-8-4007-1171-8/24/10

Keywords

BioFET, ctDNA, Debye screening, nonspecific adsorption, low-frequency noise, intrabody nanonetworks, early disease detection

ACM Reference Format:

Ida Kleger-Rudomin, Filip Lemic, Sergi Abadal, Eduard Alarcón, and Ethungshan Shitiri. 2026. Whole-Blood Boundary Analysis of BioFET-Based ctDNA Detection for Intravascular Sensing in Intrabody Nanonetworks. In *International Conference on Nanoscale Computing and Communication (NanoCom '26)*, September 21–23, 2026, St. John's, Canada. ACM, New York, NY, USA, 7 pages.

1 Introduction

Early-stage cancer detection is important in oncology because outcomes improve when cancers are identified earlier, yet many are still diagnosed at advanced stages [34, 10, 20]. This need has increased interest in blood-based molecular diagnostics that aim to detect rare tumor-derived alterations in noisy clinical backgrounds. Liquid biopsy has therefore emerged as an important route to diagnosis and monitoring by enabling access to tumor-derived material from blood without invasive tissue procedures [20, 22, 30, 4]. Among liquid-biopsy analytes, circulating tumor DNA (ctDNA) is especially informative because it carries cancer-specific genetic alterations and supports quantitative tracking of disease dynamics [38]. The most demanding applications require detecting ctDNA at very low fractions amid a large background of non-tumor cell-free DNA (cfDNA), especially in early-stage disease and after treatment [22, 30]. In this regime, performance depends on mean signal level, counting uncertainty, and background interference. These factors increase assay burden and motivate sensing strategies that can reduce reliance on intermittent laboratory measurements [5].

One response to this burden is to move sensing closer to the physiological site of interest so that molecular events can be detected *in situ* rather than inferred only from intermittent laboratory assays. Intrabody nanonetworks provide the broader systems context for this direction. In that framework, nanosensors detect local biochemical events and produce signals that can, in principle, be digitized and reported under tight size, power, and duty-cycling constraints [2]. Within that framework, intravascular sensing is especially relevant for ctDNA because blood carries the target and offers direct physiological access [29]. This study evaluates the separation between nanosensor responses with ctDNA present and target-absent whole-blood responses under physiological screening, background interference, and device noise. Fig. 1 summarizes this

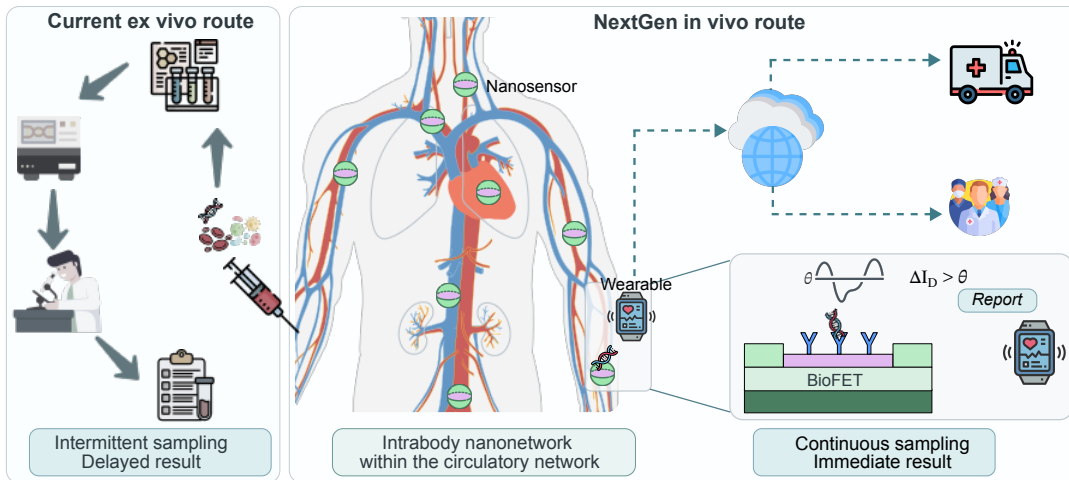


Figure 1: Whole-blood ctDNA sensing in an intrabody nanonetwork compared with conventional liquid biopsy.

intrabody setting and the bottlenecks that motivate the exploration undertaken here.

Biological field-effect transistors (BioFETs) are transistor-based nanosensors in which biomolecular binding at a functionalized surface changes the local electrostatic potential and shifts the channel current [21]. In the intravascular sensing setting, BioFETs are relevant because they are label-free, electrically integrated, and have already shown strong ctDNA sensitivity in buffer and serum [19, 25]. Their direct operation in whole blood remains strongly constrained because short Debye length, charge-to-channel separation caused by the interface stack, nonspecific adsorption, and intrinsic low-frequency noise can interfere with the signal [31, 18, 14, 16].

Work on high-ionic-strength and complex media has used local screening control, alternative measurement schemes, and interface engineering to recover charge coupling or measurement stability [15, 9, 6]. Recent studies have moved toward whole-blood BioFET operation through upstream matrix handling or analyte-specific architectures [31, 3, 27]. The broader whole-blood sensing literature also shows that intravascular operation is possible for selected analytes and mechanisms. Electrochemical aptamer-based sensors avoid Debye screening and have enabled seconds-resolved in vivo molecular measurements in circulating blood [13]. Enzyme amperometric sensors support long-duration metabolic monitoring in vivo [35]. Fiber-optic photoacoustic sensors have demonstrated intravascular whole-blood sensing for analytes such as dissolved gases and heparin [39]. We therefore use BioFET as a charge-based reference platform whose controlled-media ctDNA sensitivity and electrical compatibility make it informative for a whole-blood boundary analysis, while recognizing that direct whole-blood ctDNA sensing remains unestablished across platforms.

We address this transfer question with a reduced-order stochastic simulation model for BioFET-based ctDNA sensing under practical whole-blood conditions. The model links operating-point selection, interface geometry, finite-capacity binding, screened transduction, background response, noise, and threshold-based detection in a single local-sensing pipeline. The main contributions are as follows.

- We define intravascular ctDNA sensing as a blank-threshold detection problem under intrabody-compatible local sensing constraints, where detection depends on separation between target-present responses and target-absent whole-blood blank responses.
- We develop a reduced-order stochastic simulation model that combines analytical BioFET charge coupling and blank-threshold detection with Monte Carlo sampling of target binding, cfDNA-like background fragments, and intrinsic current noise.
- We quantify how oxide thickness, effective binding distance, ionic screening, and target concentration shape the transfer from controlled-media BioFET sensitivity to whole-blood detection performance, including regimes where high specificity coexists with weak sensitivity.

The remainder of the paper is organized as follows. Section 2 presents the stochastic end-to-end system model linking ctDNA concentration to drain-current shifts and binary detection outcomes. Section 3 reports simulation results on screening-limited signal formation, sensitivity and specificity across interface and screening regimes, and the low-frequency noise floor that compresses the margin between target-present and blank responses. Section 4 then discusses the implications of these results, the model limitations, and design directions for future work.

2 ctDNA Sensing Model

We define a reduced-order, quasi-static stochastic simulation model that maps ctDNA concentration in whole blood to a drain-current shift and a binary detection outcome. The model focuses on the local sensing stage. Device-specific implementation details and the intrabody reporting chain are outside the present scope. Fig. 2 highlights the modeled sensing stack and the whole-blood environment considered here. The model has four stages. First, it sets the operating point and baseline current. Second, it models surface occupancy by target and background fragments. Third, it converts bound charge into a Debye-screened current shift. Fourth, it estimates a blank-derived threshold and computes sensitivity and specificity. The term *blank* refers to measurements performed in the absence of

target molecules, so the response reflects only background and noise contributions.

2.1 Operating Point and Baseline Current

We first determine the electrical operating point because the sensing model measures current deviations from that baseline. The BioFET is evaluated at fixed bias voltages $V_{SG} = 0.3$ V and $V_{SD} = 0.1$ V. In the present model, these biases define a fixed operating point, and surface-potential changes are converted into drain-current shifts through the operating-point transconductance g_m [1, 21]. Let $I_{D,0}$ denote the baseline drain current at (V_{SG}, V_{SD}) in the absence of sensing effects. The measured drain current is therefore written as

$$I_D = I_{D,0} + \Delta I_D + \eta_I, \quad (1)$$

where I_D is the measured drain current, ΔI_D is the current shift, and η_I is the intrinsic current-noise term, defined in Section 2.4.

2.2 Sensing Interface and Finite-Capacity Occupancy

We next model the biofunctionalized surface. In whole blood, ctDNA recognition occurs alongside cfDNA, proteins, and other background molecules. The BioFET therefore responds to both specific ctDNA binding and nonspecific adsorption, meaning unwanted binding by non-target molecules. Passivation can reduce nonspecific adsorption and delay biofouling, which is the gradual formation of an adsorption layer that blocks binding sites, shifts surface charge, and introduces time-dependent drift [14, 36]. For nucleic-acid targets such as ctDNA, selectivity is typically provided by aptamers or ssDNA probes designed for mutation-level discrimination [33, 19].

In practice, the interface forms a multilayer stack that includes a linker or anchoring chemistry, an antifouling or passivation layer, and the bioreceptor itself [24, 26]. This stack creates the main interface tradeoff in the model. Passivation suppresses background adsorption at the cost of increasing the distance between target charge and the transducer. Under physiological screening, that added distance weakens electrostatic coupling [18]. Thinner and less passivated interfaces can increase coupling, although they are more exposed to nonspecific adsorption and drift. For charge-based sensing, even a thin adsorption layer can shift the apparent baseline because the transistor responds to the net electrostatic boundary condition set by both specific target binding and background adsorption.

The present model captures these effects through an abstraction based on competitive surface occupancy, background charge fluctuations, and an effective interface thickness. In this abstraction, the explicit competitor class in the occupancy and charge model represents charged cfDNA-like background fragments rather than the full biochemical background of whole blood. Protein adsorption, fouling-layer growth, and other non-DNA interferences motivate the whole-blood setting. In the model, their effects enter indirectly through effective interface thickness, the blank distribution, and the detection threshold. The resulting geometric quantity is the effective binding distance

$$d_{\text{eff}} = t_{\text{ox}} + d_b, \quad (2)$$

where t_{ox} is the oxide thickness and d_b is the total biofunctional-layer thickness above the oxide, including the linker or silanization

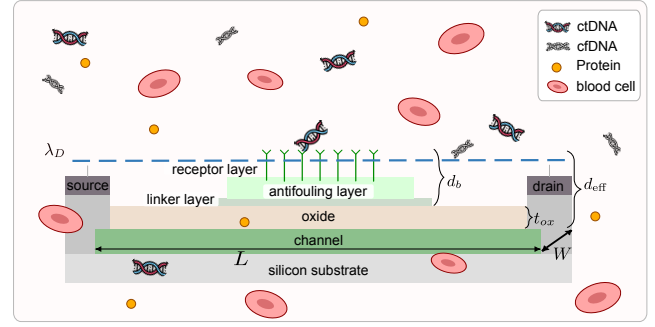


Figure 2: BioFET stack and whole-blood background modeled in Section 2.

layer, the antifouling layer, and the receptor layer. This quantity links interface design directly to screening loss in the next stage of the model.

The sensing area determines the maximum number of bound molecules that can contribute to the signal. Let W and L denote the channel width and channel length, respectively. Under a planar-area approximation, the active sensing area is $A = WL$. In the present implementation, we use the same area for electrostatic coupling. With receptor surface density ρ_R , the number of available binding sites is

$$N_R = \rho_R A. \quad (3)$$

Finite N_R imposes a hard capacity limit at the sensing interface and prevents unrealistically large current shifts at higher target concentrations [24, 37].

Next, transport and binding are represented as a stochastic finite-capacity site-assignment process. This reduced description captures occupancy at the decision time through a lumped assignment model, with full reaction kinetics and interface evolution left outside the present scope. Uncertainty therefore enters through molecule counts, intrinsic binding weights, and the finite number of receptor sites. Let N_T and N_C denote the numbers of target and background fragments in the considered exposure volume. Let C_t and C_c denote the target and background concentrations, respectively, where C_c refers to the concentration of cfDNA-like charged background fragments. Over the decision window, the model converts these concentrations into expected molecule counts, $\bar{N}_T = C_t V_{\text{sample}} N_A$ and $\bar{N}_C = C_c V_{\text{sample}} N_A$, such that $N_T \sim \text{Poisson}(\bar{N}_T)$ and $N_C \sim \text{Poisson}(\bar{N}_C)$. Here N_A denotes Avogadro's constant. V_{sample} is the effective whole-blood exposure volume used to convert concentration into expected molecule counts over the decision window. It represents cumulative exposure opportunities during that window. The Poisson step represents stochastic arrival opportunities during the decision window, rather than full transport and reaction kinetics.

Each molecule is then assigned a dimensionless binding weight. Target weights are sampled from $u_t \sim \mathcal{U}(0, 1)$, and background weights are sampled from $u_c \sim \mathcal{U}(0, 0.5)$. This gives target fragments higher expected binding weights than background fragments without introducing explicit kinetic constants. Target and background fragment lengths are drawn from fixed ranges, with $N_{bp}^{(t)} \in [50, 250]$ [33] and $N_{bp}^{(c)} \in [180, 360]$ [28]. These ranges

are implementation choices for regime comparison, not fitted fragment distributions. Surface occupation then proceeds under the finite-capacity constraint. As occupancy increases, the probability of an additional binding event is scaled by the remaining free-site fraction. The resulting bound counts K_t and K_c enter the charge-transduction stage. Under this interpretation, the model compares relative operating regimes rather than absolute reaction constants.

2.3 Debye-Screened Charge-to-Current Transduction

Electrostatic screening determines how strongly bound charge couples to the channel. The Debye length λ_D sets the range over which charge can influence the surface potential. Under physiological ionic strength, λ_D is on the order of a nanometer, so charges separated from the channel by several nanometers are strongly attenuated [18, 7]. We model this attenuation as

$$\alpha(\lambda_D, d_{\text{eff}}) = \exp\left(-\frac{d_{\text{eff}}}{\lambda_D}\right). \quad (4)$$

This term makes the geometry dependence explicit because the same bound charge produces a much smaller electrical effect when $d_{\text{eff}} \gg \lambda_D$.

Each bound molecule contributes a surface-potential shift determined by its charge content and fragment length. Let $N_{bp,n}$ denote the number of base pairs in the n -th bound molecule and let z_n denote an effective class-dependent charge multiplier that scales the nominal per-base-pair charge in the lumped model. In the present implementation, $z_n = z_t$ for target fragments and $z_n = z_c$ for cfDNA-like background fragments, with $(z_t, z_c) = (1, 0.5)$. The planar model uses a lumped interfacial capacitance density C_{eff} to convert bound charge into surface-potential shift. The oxide capacitance density is C_{ox} , and the double-layer capacitance density is C_{dl} . With effective electrolyte permittivity ε and elementary charge q , we write

$$C_{\text{eff}} = (C_{\text{ox}}^{-1} + C_{\text{dl}}^{-1})^{-1}, \quad C_{\text{dl}} = \frac{\varepsilon}{\lambda_D}, \quad (5)$$

so the oxide and double-layer terms enter through one lumped areal capacitance. In this lumped charge-coupling model, the unscreened surface-potential shift is

$$\Delta\psi_n = \frac{z_n q N_{bp,n}}{A C_{\text{eff}}}. \quad (6)$$

Eq. (6) treats the charge of a bound DNA fragment as if it acted at a single effective distance from the channel. This treatment retains the leading screening effect without representing the full spatial charge distribution explicitly [8, 17, 11]. The screened current shift is then

$$\Delta I_D = g_m \sum_{n=1}^{K_t + K_c} \Delta\psi_n \alpha(\lambda_D, d_{\text{eff}}). \quad (7)$$

Because detection uses current-shift magnitude, we report the noise-free signal amplitude as $|\Delta I_D|$. The measured shift used in detection is $\Delta I_D^{\text{meas}} = \Delta I_D + \eta_I$. This completes the measurement model.

2.4 Blank-derived Threshold Detection

We formulate detection as a binary hypothesis test on the magnitude of the sensing-induced current shift. In the absence of target

molecules, the noise-free current shift arises from background fragments. The practical question at ultra-low target concentration is whether the distribution of $|\Delta I_D^{\text{meas}}|$ with target present can be distinguished from the corresponding blank distribution.

The intrinsic electrical floor is attributed to thermal noise and low-frequency $1/f$ noise, which dominate BioFET operation in the present low-frequency regime [12, 23]. The measured current noise is modeled as a zero-mean Gaussian term, $\eta_I \sim \mathcal{N}(0, I_{n,\text{rms}}^2)$, where $I_{n,\text{rms}}$ is obtained by integrating the total current-noise PSD over the measurement band $[f_{\text{min}}, f_{\text{max}}]$.

Let N_0 denote the number of blank realizations used to estimate the threshold. The total sensing-induced current shift is $\Delta I_D = \Delta I_t + \Delta I_c$, where ΔI_t and ΔI_c are the target-induced and background-fragment-induced current shifts. In blank realizations, $\Delta I_t = 0$, so the measured blank shift is $\Delta I_{\text{blank}}^{\text{meas}} = \Delta I_c + \eta_I$. The detection threshold θ is set using a Gaussian approximation to the upper one-sided 95th percentile of the blank-shift magnitudes. In the implementation, θ is computed as the mean blank magnitude plus 1.645 times its standard deviation [32]. For each simulated operating regime, this threshold is estimated from the corresponding blank realizations and then held fixed for target-present trials in that regime.

Let M denote the number of sensors. A sensor-level detection event is declared when

$$\delta_{i,m} = \mathbb{1}\{|\Delta I_{D,i,m}^{\text{meas}}| > \theta\}, \quad (8)$$

where $\delta_{i,m} \in \{0, 1\}$ is the binary decision of sensor m in Monte Carlo realization i , and each realization represents one simulated exposure window. OR fusion across the M sensors gives the realization-level decision,

$$\hat{y}_i = \mathbb{1}\left\{\sum_{m=1}^M \delta_{i,m} \geq 1\right\}, \quad (9)$$

where $\hat{y}_i \in \{0, 1\}$ denotes the final binary decision for realization i .

With the realization-level decisions defined, sensitivity and specificity follow directly from the target-present and blank realizations. Sensitivity is the fraction of target-present realizations with $\hat{y}_i = 1$. Specificity is one minus the fraction of blank realizations with $\hat{y}_i = 1$, where $\hat{y}_i = 1$ is a false positive in the blank condition. With N_1 target-present realizations and N_0 blank realizations, we compute

$$\text{Sensitivity} = 100 \cdot \frac{1}{N_1} \sum_{i=1}^{N_1} \hat{y}_i, \quad \text{Specificity} = 100 \cdot \left(1 - \frac{1}{N_0} \sum_{i=1}^{N_0} \hat{y}_i\right). \quad (10)$$

These metrics are used throughout Section 3 to summarize detection performance.

3 Simulation Results and Analysis

All simulations were implemented in MATLAB R2025b using the model defined in Section 2. Table 1 lists the parameters used in the reported simulations. In each sweep, the swept variable is varied while the remaining parameters are fixed to the values in Table 1. Because the binding weights are phenomenological rather than fitted kinetic parameters, the results should be interpreted as comparisons across operating regimes under the stated assumptions.

Table 1: Simulation parameters.

| Parameter | Value |
|---|---|
| Operating drain bias, V_{SD} | 0.1 V |
| Operating gate bias, V_{SG} | 0.3 V |
| Transconductance, g_m | 1.42×10^{-7} S |
| Baseline drain current, $I_{D,0}$ | 1.571×10^{-6} A |
| Channel width, W | 670 nm |
| Channel length, L | 1 μ m |
| Oxide thickness, t_{ox} | 2 nm to 5 nm |
| Biofunctional-layer thickness, d_b | 1 nm to 9 nm [15, 18] |
| Receptor surface density, ρ_R | $\sim 1 \times 10^{12}$ cm $^{-2}$ [24] |
| Target concentration, C_t | 0.1 aM to 1 fM [33] |
| Background fragment concentration, C_c | 1 fM [28] |
| Effective charge multipliers, z_t, z_c | (1, 0.5) |
| Debye length, λ_D | 0.7 nm to 1.5 nm [18] |
| Effective whole-blood exposure volume, V_{sample} | 100 mL |
| Bandwidth, $[f_{min}, f_{max}]$ | (1 Hz, 1000 Hz) |
| Number of sensors, M | 2 |
| Number of Monte Carlo, N | 1000(= $N_0 = N_1$) |

3.1 Screening-limited Signal Analysis

Fig. 3 isolates screening-limited signal formation at $C_t = 0.1$ aM. For all three interface thicknesses, $|\Delta I_D|$ increases with λ_D because weaker screening allows more bound charge to modulate the channel. The separation among the curves shows that biofunctional-layer thickness strongly controls signal size. Increasing d_b from 5 nm to 7 nm and 9 nm reduces the current shift by about one to two orders of magnitude across the plotted range. The loss is largest at short Debye length, where a few extra nanometers place the charge farther outside the effective coupling range. Thus, interface distance can suppress the signal before thresholding and electronic noise are considered. This trend agrees with prior observations that high ionic strength and long charge-to-channel separation strongly weaken charge-based BioFET sensing [15, 31, 18].

Fig. 4 translates that signal trend into detection performance. Sensitivity increases sharply with λ_D , but only at sufficiently high target concentration. At 1 fM, sensitivity rises from about 30% at $\lambda_D = 0.7$ nm to near 100% once λ_D reaches about 0.8 to 0.9 nm. At 100 aM, sensitivity remains near 10% to 15%. At 10 aM, sensitivity stays close to zero. This pattern shows a threshold-like operating transition. Higher-concentration cases clear the blank-derived threshold when electrostatic coupling is strong enough, whereas lower-concentration cases remain limited by screening, background binding, and intrinsic noise.

3.2 Sensitivity and Specificity Analysis

Fig. 5 shows how oxide scaling depends on biofunctional-layer thickness under strong screening with $\lambda_D = 0.7$ nm. For $d_b = 5$ nm, reducing t_{ox} mainly improves the 1 fM case. Sensitivity falls from near 100% at $t_{ox} = 2$ nm to about 10% to 15% at $t_{ox} = 5$ nm, while 100 aM and 10 aM remain low across the sweep. For $d_b = 7$ nm, sensitivity drops sharply across all three concentrations. The comparison between Fig. 5(a) and Fig. 5(b) shows that thinning the biofunctional layer gives a larger gain than thinning the oxide alone.

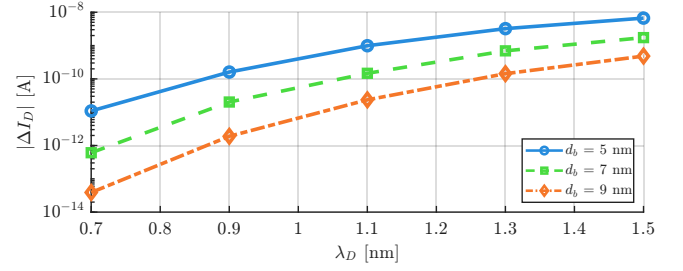


Figure 3: Signal amplitude $|\Delta I_D|$ versus λ_D for varying values of d_b with $t_{ox} = 3.5$ nm and $C_t = 0.1$ aM.

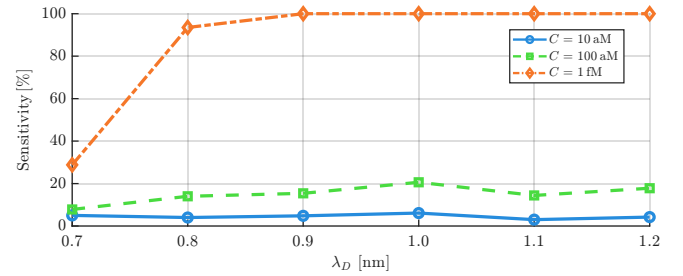


Figure 4: Sensitivity versus λ_D for three target concentrations with $t_{ox} = 3.5$ nm and $d_b = 5$ nm.

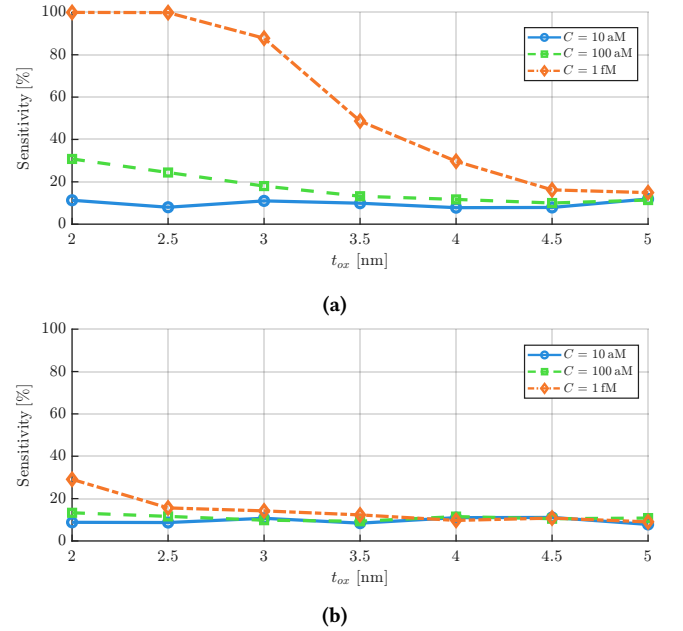


Figure 5: Sensitivity versus t_{ox} for varying target concentrations with $\lambda_D = 0.7$ nm and (a) $d_b = 5$ nm, (b) $d_b = 7$ nm.

Fig. 6 repeats the oxide-thickness sweep at $\lambda_D = 1$ nm. Sensitivity is higher and less dependent on t_{ox} than in Fig. 5(a). The 1 fM case remains near 100% across the sweep, the 100 aM case stays around 30%, and the 10 aM case remains low. Together, Figs. 5 and 6 show that oxide scaling matters most when the effective charge distance

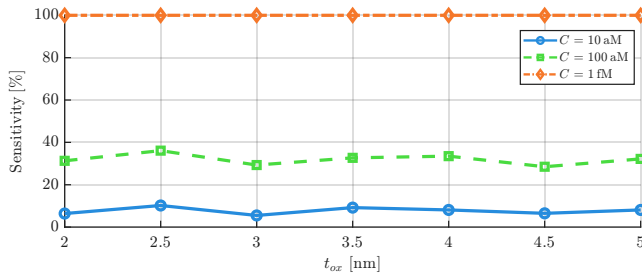


Figure 6: Sensitivity versus t_{ox} for varying target concentrations with $d_b = 5$ nm and $\lambda_D = 1$ nm.

is close to the Debye length. When screening is too strong or the interface stack is too thick, sensitivity remains low even after oxide thinning.

Fig. 7 shows that specificity stays near 90% to 93% across the oxide-thickness sweep. The blank-derived threshold therefore controls false positives in the modeled geometry range. The main loss appears instead as missed detections at low target concentration, where target-present shifts do not consistently exceed the blank floor. This pattern is consistent with the detector definition in Section 2.4, where θ is estimated from blank realizations and sensitivity depends on how often the target-present shift exceeds that blank floor.

High specificity together with weak sensitivity points to a small margin between target-present responses and the blank floor. Section 3.3 examines how intrinsic electronic noise further compresses that margin.

3.3 Low-frequency Noise Analysis

Fig. 8 shows the electronic noise floor used in the detection model. The thermal component is nearly flat across frequency, whereas the $1/f$ component is much larger at low frequency and decreases gradually with frequency. Because the model uses a quasi-static low-frequency regime, flicker noise dominates most of the measurement band. This explains why weak screened signals remain difficult to detect. After screening and interface distance reduce the signal margin, blank fluctuations and low-frequency electronic noise can keep the measured current shift below the decision threshold. Taken together, Figs. 3 to 8 show that whole-blood BioFET detection is limited by electrostatic screening, charge-to-channel separation, blank-response fluctuations, and low-frequency noise.

4 Conclusions and Future Work

This study shows that BioFET-based ctDNA sensitivity in controlled media does not carry over directly to whole-blood intravascular sensing. In the tested quasi-static charge-gating regime, short Debye length, several-nanometer charge-to-channel separation, background fluctuations, and low-frequency noise reduce the separation between target-present and blank responses. Under strong screening and thicker interface conditions, the lower end of the tested concentration range rarely exceeds the blank-derived threshold, while 1 fM reaches high sensitivity only under more favorable screening.

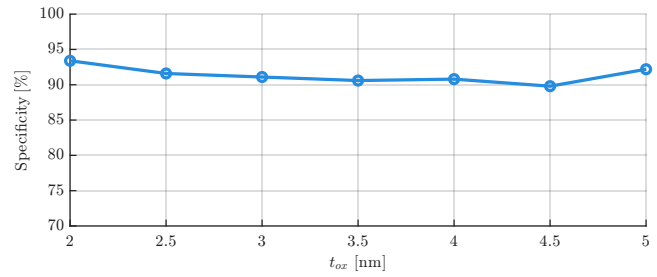


Figure 7: Specificity versus t_{ox} with $d_b = 5$ nm and $\lambda_D = 0.7$ nm.

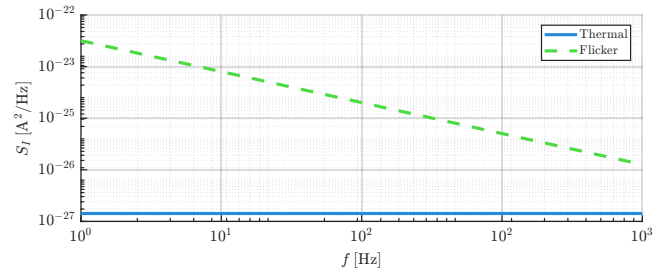


Figure 8: Thermal and $1/f$ current noise power spectral density for $t_{ox} = 3.5$ nm.

The model remains simplified because it focuses on boundary behavior rather than full device reproduction. It omits time-dependent transport and binding kinetics, additional noise and drift mechanisms, fabrication fluctuations, and threshold sweeps across the full target-present and blank distributions. The absolute sensitivity values also depend on the effective exposure volume and the phenomenological binding-weight ranges, so the reported curves should be read as regime comparisons rather than fitted predictions for a specific receptor chemistry. Future work should test whether thinner interface stacks, improved surface chemistries, alternative device structures, or different threshold choices can widen the separation between target-present and blank responses. More broadly, closing the ctDNA whole-blood gap may require interface improvements within the BioFET architecture and closer examination of transduction principles that avoid electrostatic field gating in physiological electrolytes. For intrabody nanonetworks, the key takeaway is that local sensing performance must be evaluated in whole blood. In the BioFET case studied here, physiological screening, interface distance, background binding, and noise can reduce the target signal enough to limit reliable ctDNA detection.

Acknowledgments

This project has received funding from the European Union's Horizon Europe research and innovation programme under the Marie Skłodowska-Curie grant agreement No. 101154851.

References

- [1] Jae-Hyuk Ahn et al. 2017. Charge and dielectric effects of biomolecules on electrical characteristics of nanowire FET biosensors. *Applied Physics Letters*, 111, 113701. doi:10.1063/1.5003106.
- [2] I. F. Akyildiz et al. 2015. The internet of Bio-Nano things. *IEEE Communications Magazine*, 53, 3, 32–40. doi:10.1109/MCOM.2015.7060516.

- [3] Shubham Babbar et al. 2026. Reassessing the challenge of Debye length in field-effect biosensors. *Chemical Engineering Journal*, 527, 172070. doi:10.1016/j.cej.2025.172070.
- [4] Chetan Bettgowda et al. 2014. Detection of circulating tumor DNA in early- and late-stage human malignancies. *Science Translational Medicine*, 6, 224, 224ra24–224ra24. eprint: <https://www.science.org/doi/pdf/10.1126/scitranslmed.3007094>. doi:10.1126/scitranslmed.3007094.
- [5] P. Bittla et al. 2023. Exploring circulating tumor DNA (ctDNA) and its role in early detection of cancer: a systematic review. *Cureus*, 15, 9, (Sept. 2023), e45784. doi:10.7759/cureus.45784.
- [6] Duo Chen et al. 2024. Nanostructured interface-engineered field-effect transistor biosensors for sensitive detection of serum miRNAs. *The Innovation Materials*, 2, 4, 100091. doi:10.59717/j.xinn-mater.2024.100091.
- [7] H. Chen et al. 2019. A new biosensor detection system to overcome the Debye screening effect: dialysis-silicon nanowire field effect transistor. *International Journal of Nanomedicine*, 14, (Apr. 2019), 2985–2993. doi:10.2147/IJN.S198734.
- [8] Tim Cholko, Shivansh Kaushik, and Chia-En A. Chang. 2019. Dynamics and molecular interactions of single-stranded DNA in nucleic acid biosensors with varied surface properties. *Physical Chemistry Chemical Physics*, 21. doi:10.1039/C9CP02441G.
- [9] Chia-Ho Chu et al. 2017. Beyond the Debye length in high ionic strength solution: direct protein detection with field-effect transistors (FETs) in human serum. *Scientific Reports*, 7, 1, 5256. doi:10.1038/s41598-017-05426-6.
- [10] D. Crosby et al. 2022. Early detection of cancer. *Science*, 375, eaay9040. doi:10.1126/science.aay9040.
- [11] Luca De Vico et al. 2011. Predicting and rationalizing the effect of surface charge distribution and orientation on nano-wire based FET bio-sensors. *Nanoscale*, 3, 9, 3635–3640. doi:10.1039/C1NR10316D.
- [12] M. Jamal Deen et al. 2006. Noise considerations in field-effect biosensors. *Journal of Applied Physics*, 100, 7, 074703. doi:10.1063/1.2355542.
- [13] Alex M. Downs and Kevin W. Plaxco. 2022. Real-time, in-vivo molecular monitoring using electrochemical aptamer-based sensors: opportunities and challenges. *ACS Sensors*, 7, 10, 2823–2832. doi:10.1021/acssensors.2c01428.
- [14] Andreas Frutiger et al. 2021. Nonspecific binding—fundamental concepts and consequences for biosensing applications. *Chemical Reviews*, 121, 13, 8095–8160. doi:10.1021/acs.chemrev.1c00044.
- [15] Ning Gao et al. 2015. General strategy for biodetection in high ionic strength solutions using transistor-based nanoelectronic sensors. *Nano Letters*, 15, 3, 2143–2148. doi:10.1021/acs.nanolett.5b00133.
- [16] Lusine Gasparyan, Ferdinand Gasparyan, and Vahan Simonyan. 2021. Internal electrical noises of BioFET sensors based on various architectures. *Open Journal of Biophysics*, 11, (Jan. 2021), 177–204. doi:10.4236/ojbiophys.2021.112006.
- [17] Eric A. Josephs and Tao Ye. 2012. Electric-field dependent conformations of single DNA molecules on a model biosensor surface. *Nano Letters*, 12, 10, 5255–5261. doi:10.1021/nl3024356.
- [18] Vladimir Kesler, Boris Murmann, and H. Tom Soh. 2020. Going beyond the Debye length: overcoming charge screening limitations in next-generation bioelectronic sensors. *ACS Nano*, 14, 12, 16194–16201. doi:10.1021/acsnano.0c08622.
- [19] Dujuan Li et al. 2021. A supersensitive silicon nanowire array biosensor for quantitating tumor marker ctDNA. *Biosensors and Bioelectronics*, 181, 113147. doi:10.1016/j.bios.2021.113147.
- [20] X. Liang et al. 2025. Liquid biopsy: a breakthrough technology in early cancer screening. *Cancer Screening and Prevention*, 4, 1, 40–52. doi:10.14218/CSP.2024.00031.
- [21] Benjamin Lowe et al. 2017. Field-effect sensors – from pH sensing to biosensing: sensitivity enhancement using streptavidin-biotin as a model system. *The Analyst*, 142. doi:10.1039/C7AN00455A.
- [22] Liwei Ma et al. 2024. Liquid biopsy in cancer: current status, challenges and future prospects. *Signal Transduction and Targeted Therapy*, 9, 1, (Dec. 2024), 336. doi:10.1038/s41392-024-02021-w.
- [23] Carlos Augusto Bergfeld Mori et al. 2022. Signal to noise ratio in nanoscale BioFETs. *Solid-State Electronics*, 194, 108358. doi:10.1016/j.sse.2022.108358.
- [24] Jacopo Movilli et al. 2018. Control of probe density at DNA biosensor surfaces using poly(L-lysine) with appended reactive groups. *Bioconjugate Chemistry*, 29, 12, 4110–4118. doi:10.1021/acs.bioconjchem.8b00733.
- [25] Xia Peng et al. 2025. Signal-to-noise enhanced detection of circulating tumor DNA via rolling circle amplification and amphiphilic polymer-integrated field-effect transistor sensors. *Microchemical Journal*, 217, 114981. doi:10.1016/j.micr.2025.114981.
- [26] Toshiya Sakata. 2024. Signal transduction interfaces for field-effect transistor-based biosensors. *Communications Chemistry*, 7, 1, 35. doi:10.1038/s42004-024-01121-6.
- [27] Soumabri Samanta et al. 2026. Biological transistors for direct biosensing of L-Dopa in ultrasmall samples of unprocessed and unwashed whole blood. *ACS Sensors*, 11, 1, 107–118. doi:10.1021/acssensors.5c02466.
- [28] Jiping Shi et al. 2020. Size profile of cell-free DNA: a beacon guiding the practice and innovation of clinical testing. *Theranostics*, 10, 11, 4737–4748. doi:10.7150/t.42565.
- [29] Ethungshan Shitiri et al. 2024. Work-in-progress: intra-body nanonetworks for in vivo biomarker detection in capillaries. In *Proceedings of the 11th Annual ACM International Conference on Nanoscale Computing and Communication (NANOCOM '24)*. Association for Computing Machinery, Milan, Italy, 134–135. ISBN: 9798400711718. doi:10.1145/3686015.3689424.
- [30] Giulia Siravegna et al. 2017. Integrating liquid biopsies into the management of cancer. *Nature Reviews Clinical Oncology*, 14, 9, 531–548.
- [31] Eric Stern et al. 2010. Label-free biomarker detection from whole blood. *Nature Nanotechnology*, 5, 2, 138–142. doi:10.1038/nnano.2009.353.
- [32] Mohamad T. 2018. Limit of Blank (LOB), Limit of Detection (LOD), and Limit of Quantification (LOQ). *Organic & Medicinal Chemistry International Journal*, 7, 5, 555722. doi:10.19080/OMCIJ.2018.07.555722.
- [33] X. Wen et al. 2022. Circulating tumor DNA—a novel biomarker of tumor progression and its favorable detection techniques. *Cancers*, 14, 24, 6025. doi:10.3390/cancers14246025.
- [34] World Health Organization. 2025. Cancer. [Accessed: 13-Feb-2026]. https://www.who.int/health-topics/cancer#tab=tab_1.
- [35] Jie Wu et al. 2023. Device integration of electrochemical biosensors. *Nature Reviews Bioengineering*, 1, 5, 346–360. doi:10.1038/s44222-023-00032-w.
- [36] Jian Xu and Hyowon Lee. 2020. Anti-biofouling strategies for long-term continuous use of implantable biosensors. *Chemosensors*, 8, 3, 66. doi:10.3390/chemosensors8030066.
- [37] Shicai Xu et al. 2017. Real-time reliable determination of binding kinetics of DNA hybridization using a multi-channel graphene biosensor. *Nature Communications*, 8, 14902. doi:10.1038/ncomms14902.
- [38] Kexin Yi et al. 2023. Emerging ctDNA detection strategies in clinical cancer theranostics. *Smart Medicine*, 2, 4, e20230031. doi:10.1002/SMD.20230031.
- [39] Jingcheng Zhou et al. 2022. A fiber optic photoacoustic sensor for real-time heparin monitoring. *Biosensors and Bioelectronics*, 196, 113692. doi:10.1016/j.bios.2021.113692.